Curing-Induced Residual Stress and Strain in Thermoset Composites

M. H. Nagaraj[*], M. Maiaru[†]
Department of Mechanical Engineering,
University of Massachusetts Lowell, MA 01854, United States

Corresponding Author:
Marianna Maiaru,
Department of Mechanical Engineering,
University of Massachusetts Lowell,
Lowell 01854,
MA, United States

[*]Postdoctoral Research Associate, e-mail: manish_nagaraj@uml.edu
[†]Associate Professor, e-mail: marianna_maiaru@uml.edu

Abstract

Uncontrolled curing-induced residual stress and strain are significant limitations to the efficient design of thermoset composites that compromise their structural durability and geometrical tolerance. Experimentally validated process modeling for the evaluation of processing parameter contributions to the residual stress build-up is crucial to identify residual stress mitigation strategies and enhance structural performance. This work presents an experimentally validated novel numerical approach based on higher-order finite elements for the process modeling of fiber-reinforced thermoset polymers across two composite characteristic length scales, the micro and macro-scale levels. The cure kinetics is described using an auto-catalytic phenomenological model. An instantaneous linear-elastic constitutive law, informed by time-dependent material characterization, is used to evaluate the stress state evolution as a function of the degree of cure and time. Micromechanical modeling is based on Representative Volume Elements (RVEs) that account for random fiber distribution verified against traditional 3D FE analysis. 0/90 laminate testing at the macroscale validates the proposed approach within an accuracy of 9%.

Keywords: Process modeling, curing, residual stress, micromechanics

1 Introduction

Experimentally-validated process modeling of thermoset composites is fundamental for overcoming technological challenges that will enable the full potential of the fourth industrial revolution (Industry 4.0) in advanced manufacturing [1]. Within Industry 4.0, Integrated Computational Materials Engineering (ICME) is a new paradigm for the concurrent design of materials and products that aims to create a cyber-physical ecosystem that will enable streamlining design and manufacturing and obtain accurate life and performance predictions based on digital twins starting from an accurate representation of the part during manufacturing [2]. Fiber-reinforced plastics (FRP) play a prominent role in lightweight eco-efficient transportation, including Urban Air Mobility (UAM), space exploration, automotive, and wind, due to their outstanding mechanical properties, such as specific strength and stiffness. However, their complex mechanical response and uncertainties in their properties due to manufacturing imperfections lead to the use of larger margins of safety and an overly conservative design, which restricts the utilization of the full potential of composite materials and limits structural efficiency. A further bottleneck is the ample design space associated with composite structures, which renders physical testing a lengthy and resource-intensive task.

The manufacturing process of thermoset FRP has a significant effect on both the final geometry of the part as well as its mechanical performance. The manufacturing process, or curing, consists of an exothermic chemical reaction, during which material properties change as a function of time and temperature. The thermal expansion mismatch between fibers and matrix leads to differential expansion within the composite microstructure. Such thermal expansion mismatch at the level of the constituents, in combination with chemical shrinkage of the matrix and the thermo-mechanical properties evolution during the cure cycle, results in self-equilibrated residual stresses [3, 4]. High residual stress levels during the cure cycle can lead to the formation of micro-cracks within the matrix, significantly reducing the composite mechanical performance and service life [5, 6]. The robust design and optimization of composite structures thus requires an accurate understanding of the development of residual stresses within the manufactured part.

Computationally efficient multiscale process modeling is needed to predict curing-induced residual stresses accurately [7]. Different numerical techniques can reproduce the relevant fundamental physics across the relevant scales in fiber-reinforced composites, including the evolution of the mechanical and non-mechanical properties of the matrix as a function of curing, local fiber constraint of the curing matrix, thermal gradients, and stress concentrations induced by complex tow architectures [8–13]. Recent work proved that it is possible to virtually reproduce the crosslinking formation of the polymer during curing at the nano-scale using Molecular Dynamics (MD) simulations [14, 15]. MD simulations accurately represent the chemical composition of the resin and its curing agent and predict the mechanical property evolution of the matrix as a function of the crosslinking density [16, 17]. The local variation in fiber volume fraction driven by the stochastic distribution of the fibers induces local variability in the residual stress state, which in turn affects the mechanical properties of the curing resin. Additionally, fiber closeness can act as a stress riser in the microstructure that triggers premature failure [18–20].

Modeling the micro-scale resolution enables the explicit representation of the reinforcing fibers and the resulting stochastic property variabilities within the composite constituents needed to represent a realistic structure [21–23]. Thus, the explicit modeling of the fibers at the micro-scale is crucial to predict the composite failure behavior accurately [24–28]. While traditional 3D Finite Element (3D-FE) analysis is a preferred tool to analyze complex structures at the macro-scale [29, 30], computational micromechanical models based on conventional FE can incur prohibitively high costs, especially when they are used in a multiscale setting to inform composite material behavior in a structural-level analysis [31]. Thus, a computationally-efficient numerical approach is necessary to model the microstructure, which would eventually form part of multiscale process modeling frameworks.

Several cure models have been proposed in the literature [32–34], with one of the most popular formulations being the phenomenological model by Kamal and Sourour [35]. These kinetic models have been used in various numerical investigations on the prediction of residual stresses during the curing process, as well as the influence of these stresses on the effective mechanical properties of the composite. For instance, Ding et al. proposed a 3D thermo-viscoelastic model to simulate residual stresses in composite laminates during curing [36]. Maiaru et al. investigated the influence of the manufacturing process on the transverse strength of unidirectional FRP using traditional FEs [20]. More recently, Hui et al. developed a micro-scale viscoplastic model to investigate the effect of curing-induced stresses on the compressive strength of unidirectional FRP [37]. Similarly, DMello et al. presented an approach to simulate the curing process of homogenized textile composites and subsequently evaluated the effect of the developed residual stresses on the tensile strength of the composite [30].

a unified formulation for micro and macro scale modeling

This paper presents the implementation of an instantaneous linear elastic micro-scale curing model in a computational framework based on higher-order FEs that will enable multiscale modeling of fiber-reinforced composites. Lagrange polynomials are implemented within the Carrera Unified Formulation (CUF), which is a generalized framework for developing higher-order structural theories. CUF-based models are capable of an accuracy approaching that of 3D-FEs at significantly reduced computational effort [38]. The advantages of CUF have been demonstrated in recent years for various classes of problems, such as progressive damage and impact [39–41], micromechanical analysis [42–45], and the analysis of process-induced deformations in cured composite parts [46]. The present work combines a process modeling formulation for thermoset epoxies [20, 47] with CUF theories to enable the micro-scale curing analysis of thermoset composites.

This work is organized as follows: Section 2 describes the higher-order FE structural modeling approach within CUF and the process modeling formulation. A series of numerical assessments is presented in Section 3 to verify the proposed approach using traditional FEs. The main conclusions are summarized in Section 4.

2 Numerical modeling

## 2.1 Process Modeling: Thermoset Curing

The thermoset cure kinetics, for a given cure cycle, is governed by an auto-catalytic phenomenological semi-empirical kinetic model [35], as follows

$$\frac{d\phi}{dt} = \left[A_1 exp\left(-\frac{\Delta E_1}{RT} \right) + A_2 exp\left(-\frac{\Delta E_2}{RT} \right) \phi^n \right] (1 - \phi^m) \tag{1}$$

where ϕ is the degree of cure, R is the gas constant, T is the cure temperature at time t, with the activation energies denoted by ΔE_1 and ΔE_2. The constants A_1 and A_2, and the exponents m and n, are determined experimentally. The thermal state of the thermoset is a consequence of the prescribed cure temperature and the heat generated due to the exothermic nature of the curing process, and the resulting temperature distribution is evaluated using the Fourier heat transfer model as follows

$$\rho c_p \frac{dT}{dt} = \kappa_i \frac{d^2T}{dt^2} + \frac{dq}{dt}, \; with \; \frac{dq}{dt} = \rho H_T \frac{d\phi}{dt} \tag{2}$$

where ρ and c_p are respectively the density and specific heat of the epoxy, κ_i is the thermal conductivity, q is the instantaneous exothermic heat generated during the curing process, and H_T is the total heat of reaction.
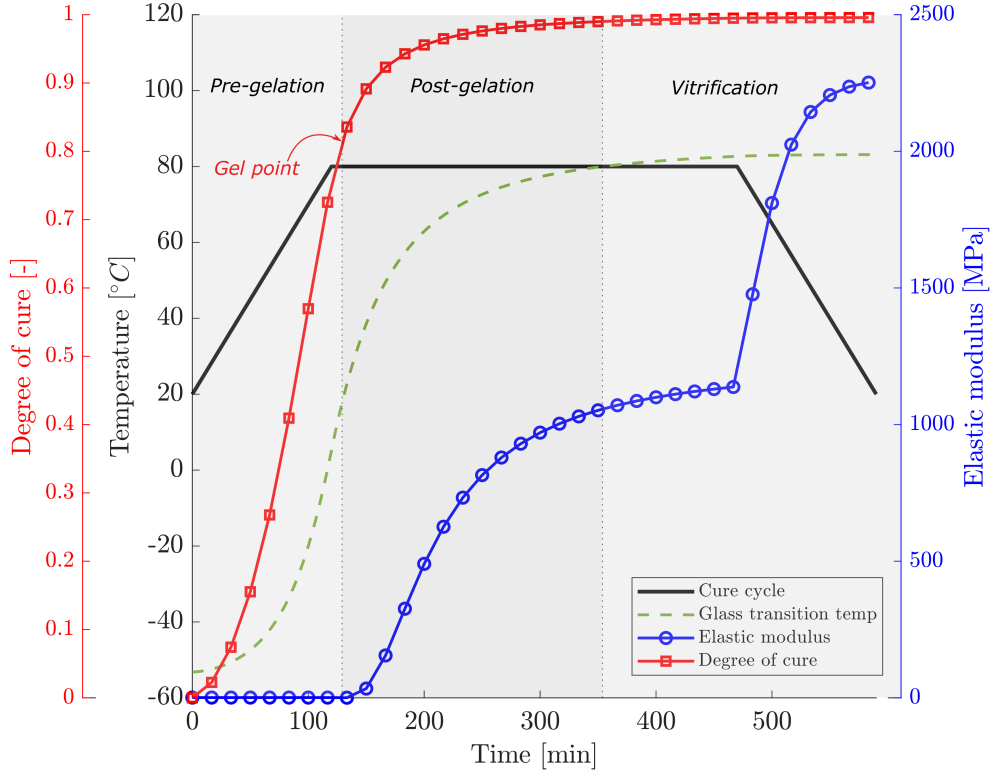
Figure 1: Temperature - degree of cure plot of RIM R135/H1366 epoxy resin system with evolution of the elastic modulus.

During the curing process, the change in the degree of cure (as a function of time) results in an evolution of the chemo-rheological and thermo-mechanical properties of the thermoset. These properties have been previously characterized in-house for the RIM R135/H1366 epoxy resin system [47], and their evolution for the manufacturer recommended cure cycle is plotted in Fig. 1. The experimentally determined cure kinetics constants for this material system, required to evaluate Eq. 1, is listed in Table 1. The evaluated degree of cure, for a specific time t, can be used to determine the material state of the thermoset as seen in Fig. 1. These properties can be used with an instantaneous linear-elastic constitutive model, previously described in Ref. [20], to predict the development of residual stresses (σ_i) as a function of the evolving thermal and chemical strains as follows

$$\sigma_i(t) = \left[C_{ij}(t) \left[\varepsilon_j^{tot}(t) - (\varepsilon_j^{therm}(t) + \varepsilon_j^{shrink}(t))\delta_j \right] \right], where \ \delta_j = \begin{cases} 1 & j = 1,2,3 \\ 0 & j > 3 \end{cases} \tag{3}$$

where $\varepsilon_j^{tot}(t)$, $\varepsilon_j^{therm}(t)$ and $\varepsilon_j^{shrink}(t)$ are respectively the total, thermal and chemical shrinkage strains, and C_{ij} is the material stiffness as a function of time.

The computational approach to simulate the curing process is developed based on the instantaneous linear-elastic nature of Eq. 3. A time-based analysis, considering an incremental time period Δt, is performed over the cure cycle seen in Fig. 1, and the degree of cure is evaluated at each time increment. The mechanical properties of the thermoset are determined as a function of the degree of cure, based on experimental characterization data. An uncoupled displacement-temperature analysis is performed to compute the displacements and temperature fields. Finally, Eq. 3 is used to predict the residual stress developed within the thermoset material.

Table 1: Cure kinetics parameters for the RIM R135/H1366 epoxy resin system [47].

Cure kinetic parameter	Value
Exponent m	0.4 $[-]$
Exponent n	1.5 $[-]$
Rate constant A_1	3.6×10^9 $[s^{-1}]$
Rate constant A_2	0.01245 $[s^{-1}]$
Activation energy ΔE_1	85.3 $[kJ/mol]$
Activation energy ΔE_2	11.1 $[kJ/mol]$

2.2 Structural modeling: Carrera Unified Formulation

The Carrera Unified Formulation (CUF) is a generalized framework to derive higher-order structural theories, and in combination with the Finite Element Method (FEM), can be used to develop higher-order numerical models. Specifically, CUF allows for the kinematic enrichment of beam (1D-CUF) and plate/shell (2D-CUF) elements by the use of additional interpolation functions, resulting in numerical models that approach the accuracy of 3D-FEA at significantly reduced computational effort.
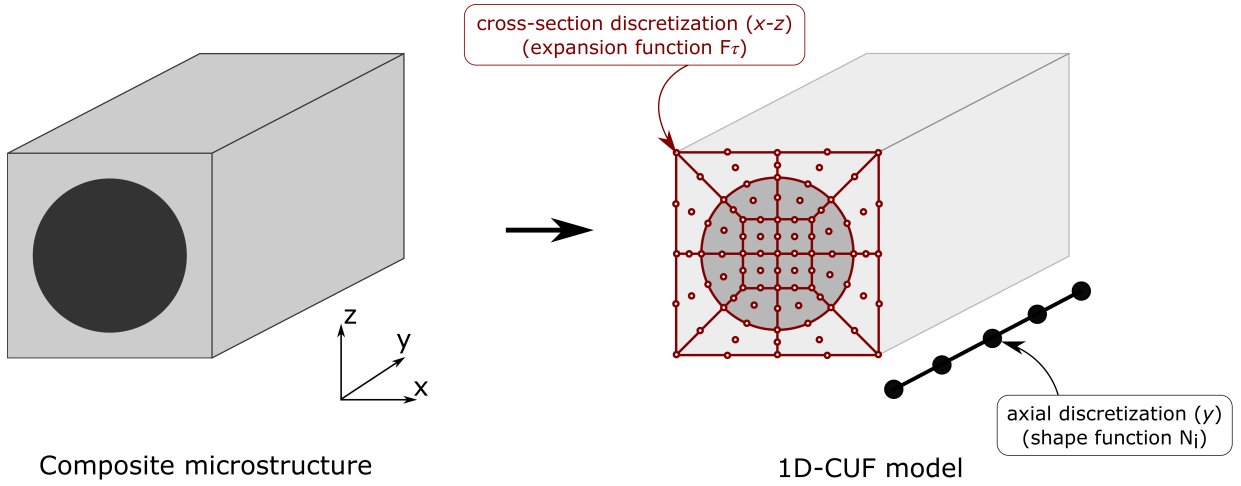
Figure 2: Modeling of a prismatic structure using 1D-CUF.

The current work uses 1D-CUF models, wherein the cross-section of beam elements is explicitly defined by a set of additional interpolation functions, termed as expansion functions (F_τ), as seen in Fig. 2. In this approach, the displacement field is defined as [38]

$$\mathbf{u} = F_\tau(x, z)\mathbf{u}_\tau(y), \ \ \tau = 1, 2, ..., M \tag{4}$$

where M is the number of terms within the expansion function. Various classes of polynomial functions can be used as (F_τ), and is chosen by the user. The most popular choice of expansion function are those based on Taylor series [48] and Lagrange polynomials [49]. Various other functions have been proposed to enhance the cross-sectional interpolation [50, 51]. The present work considers the use of Lagrange polynomials as F_τ, which consist of nodal interpolation functions within the cross-sectional discretization, see Fig. 2. This leads to a purely displacement-based formulation as seen below:

$$
\begin{aligned}
u^x &= \sum_{i=1}^{Nnode} F_i(x, z) \cdot u_i^x \\
u^y &= \sum_{i=1}^{Nnode} F_i(x, z) \cdot u_i^y \\
u^z &= \sum_{i=1}^{Nnode} F_i(x, z) \cdot u_i^z
\end{aligned}
\tag{5}
$$

where u_i^x, u_i^y, u_i^z and $F_i(x, z)$ are the translational degrees of freedom (DOF) and the interpolation function, respectively, of node i. Furthermore, the use of cross-sectional Lagrange elements allows for the explicit modeling of each component domain within the structure, and is known as Component-Wise modeling [52, 53].

Finite element formulation

The stress and strain fields are defined using the Voigt notation as follows:

$$\boldsymbol{\sigma} = \{\sigma_{xx}, \sigma_{yy}, \sigma_{zz}, \sigma_{xy}, \sigma_{xz}, \sigma_{yz}\}$$

$$\boldsymbol{\varepsilon} = \{\varepsilon_{xx}, \varepsilon_{yy}, \varepsilon_{zz}, \varepsilon_{xy}, \varepsilon_{xz}, \varepsilon_{yz}\}$$

(6)

Considering infinitesimal strain theory, the displacement-strain relationship is described using the differential operator $\mathbf{D}$ as

$$\boldsymbol{\varepsilon} = \mathbf{D}\mathbf{u} \tag{7}$$

with

$$\mathbf{D} = \begin{bmatrix} \frac{\partial}{\partial x} & 0 & 0 \\ 0 & \frac{\partial}{\partial y} & 0 \\ 0 & 0 & \frac{\partial}{\partial z} \\ \frac{\partial}{\partial y} & \frac{\partial}{\partial x} & 0 \\ \frac{\partial}{\partial z} & 0 & \frac{\partial}{\partial x} \\ 0 & \frac{\partial}{\partial z} & \frac{\partial}{\partial y} \end{bmatrix}$$

The stress-strain relation is given as

$$\boldsymbol{\sigma} = \mathbf{C}(\phi)\boldsymbol{\varepsilon} \tag{8}$$

where $\mathbf{C}$ is the 6×6 material stiffness matrix. For the case of thermoset polymers, $\mathbf{C}$ depends on the cure state which is quantified by the degree of cure (ϕ) as described in Section 2.1. Discretizing the structure, schematically shown in Fig. 2, along its axis with 1D finite elements (using interpolation functions N_i), and refining the cross-sectional kinematics using expansion functions F_τ, the 3D displacement can be written as

$$\mathbf{u}(x, y, z) = F_\tau(x, z)N_i(y)\mathbf{u}_{\tau i} \tag{9}$$

According to the principle of virtual work

$$\delta L_{int} = \delta L_{ext} \tag{10}$$

where the virtual variation of the internal strain energy δL_{int} is defined as

$$\delta L_{int} = \int_V \delta\boldsymbol{\varepsilon}^T : \boldsymbol{\sigma} \tag{11}$$

Combining Eqs. 8, 9 and 11, the stiffness matrix can be derived as

$$\delta L_{int} = \delta\mathbf{u}_{sj}^T \mathbf{k}_{ij\tau s}\mathbf{u}_{\tau i} \tag{12}$$

with

$$\mathbf{k}_{ij\tau s} = \int_l \int_A \mathbf{D}^T(N_i(y)F_\tau(x,z))\mathbf{C}(\phi)\mathbf{D}(N_j(y)F_s(x,z)) \; dA \; dl \tag{13}$$

The 3x3 matrix $\mathbf{k}_{ij\tau s}$ is the Fundamental Nucleus (FN), and its definition remains invariant with respect to any given combination of interpolation function N_i and expansion function F_τ. The element-level stiffness matrix can then be computed by assembling the fundamental nuclei associated with each combination of the nodal indices $\{i, j, \tau, s\}$. The numerical model used in the current work requires a temperature DOF, in addition to the three mechanical DOF, in order to simulate the thermoset curing process. The temperature DOF can be accounted for in the FN by considering a thermal term k_θ as follows [54]

$$k_\theta = \int_l \int_A \boldsymbol{\nabla}^T(N_iF_\tau)\kappa\boldsymbol{\nabla}(N_jF_s) \; dA \; dl \tag{14}$$

where κ is the material thermal conductivity. Considering an uncoupled temperature-displacement problem, the augmented FN is now a 4×4 matrix, defined as

$$k_{ij\tau s}^{u\theta} = \begin{bmatrix} \mathbf{k}_{ij\tau s} & \mathbf{0} \\ \mathbf{0} & \mathbf{k}_\theta \end{bmatrix} \tag{15}$$

2.3 Macroscale modeling

The structural modeling approach described in Section 2.2 is also employed in composite process modeling at the macroscopic length-scale, and enables the prediction of structural distortions after the curing and tool removal process. The cure kinetics model (see Section 2.1) is used to evaluate the resin cure state, and hence the evolving material properties, based on the applied cure cycle. The effective ply properties are then obtained by homogenization, via the ply micromechanics model by Bogetti and Gillespie [55]. Both the composite part and the mold are explicitly modeled in the process simulation to account for the effect of tool removal. A shear layer, i.e., a layer of elements with reduced shear stiffness, is used to represent the tool/part interface and allow for frictionless interaction between the tool and part [46]. At the end of the cure cycle, an additional mechanical analysis is performed to simulate the tool removal procedure and predict the final composite deformed shape after demolding [56].

Considering an increment n within the time-based process analysis, corresponding to time t_n, the mechanical problem is described as [46]

$$\mathbf{K}_n\Delta\mathbf{U}_n = \Delta\mathbf{F}_n \tag{16}$$

where $\mathbf{K}_n$ is the global stiffness matrix including contributions from the tool, composite part, and the shear layer. $\Delta\mathbf{U}_n$ is the incremental displacement as a result of the incremental thermal and shrinkage strains

represented by $\Delta \mathbf{F}_n$. The interfacial force term representing the constraint of the tool on the part can be calculated as

$$\Delta \mathbf{F}_n^{interface} = \mathbf{K}_n^{part} \Delta \mathbf{U}_n^{part} - \Delta \mathbf{F}_n^{part} \tag{17}$$

where the quantities with superscript *part* refers to components containing degrees of freedom associated with only the composite part. The incremental force terms calculated from Eq. 17 at each time-step are summed at the end of the cure analysis to obtain the total interfacial forces acting on the part as follows

$$\mathbf{F}^{interface} = \sum_{n=1}^{N_{steps}} \Delta \mathbf{F}_n^{interface} \tag{18}$$

The deformation $\mathbf{U}^*$ due to the total interface force evaluated in Eq. 18 is computed by solving the following problem

$$\mathbf{K}^{part} \mathbf{U}^* = \mathbf{F}^{interface} \tag{19}$$

The final deformed state of the composite structure, after curing and tool-removal, is obtained as

$$\mathbf{U}^{part} = \mathbf{U}^* + \sum_{n=1}^{N_{steps}} \Delta \mathbf{U}_n^{part} \tag{20}$$

3   Microscale Verification Against Traditional FEs

A series of numerical assessments is presented in this section, with the aim of verifying the proposed modeling approach, as well as to evaluate its performance with respect to conventional 3D-FEA. The micromechanical models of the fiber-reinforced epoxy are composed of IM7 fiber and RIM R135/H1366 epoxy resin, whose thermo-mechanical properties are listed in Table 2 and 3, respectively. In each case, the cure simulation follows the cure cycle plotted in Fig. 1.
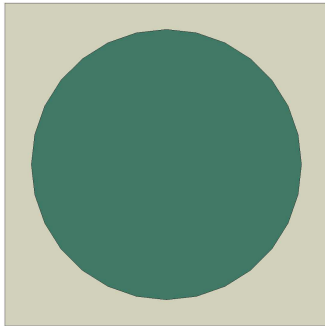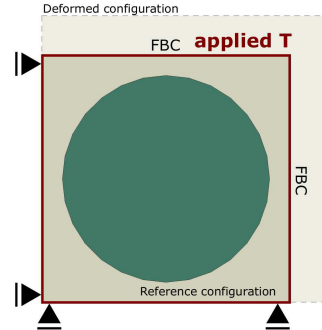
3.1   Curing of square-packed RUC

The present numerical example considers the square-packed Repeating Unit Cell (RUC) with a single fiber, as shown in Fig. 3a. The boundary conditions applied on the RUC are schematically shown in Fig. 3b. A prescribed temperature based on the cure cycle (See Fig. 1) is applied on the surface of the RUC. Flat Boundary Conditions (FBC), a special case of Periodic Boundary Conditions (PBC), are applied on the faces of the RUC which ensures that its faces remain flat in the deformed configuration. Further details on the use of FBC and its equivalence to PBC in the current application can be found in [20, 47].

Table 2: Elastic and thermal material properties of the IM7 carbon fiber [47].

Material Property	Value
Density ρ^f	1780.0 $[kg/m^3]$
Axial modulus E_{11}^f	276.0 $[GPa]$
Transverse modulus E_{22}^f, E_{33}^f	19.5 $[GPa]$
In-plane Poisson's ratio ν_{12}^f, ν_{13}^f	0.28 $[-]$
Out-of-plane Poisson's ratio ν_{23}^f	0.25 $[-]$
In-plane shear modulus G_{12}^f, G_{13}^f	70.0 $[GPa]$
Out-of-plane shear modulus G_{23}^f	7.8 $[GPa]$
Axial coefficient of thermal expansion (CTE) α_{11}^f	-0.54E-6 $[K^{-1}]$
Transverse CTE α_{22}^f, α_{33}^f	10.08E-6 $[K^{-1}]$
Thermal conductivity κ^f	5.4 $[W/mK]$
Specific heat c_p^f	879.0 $[J/kgK]$

**Table 3:** Elastic and thermal material properties of the RIM R135/H1366 epoxy resin [47].

Material Property	Value
Density ρ^m	1200.0 $[kg/m^3]$
Elastic modulus E^m	2482.0 $[MPa]$
Poisson's ratio ν^m	0.37 $[MPa]$
Coefficient of thermal expansion α^m	61.0E-6 $[K^{-1}]$
Coefficient of chemical shrinkage β^m	0.111 $[-]$
Thermal conductivity κ^m	0.245 $[W/mK]$
Specific heat c_p^m	1600.0 $[J/kgK]$

(a) Square-packed RUC

(b) Boundary conditions for curing analysis

Figure 3: Schematic representation of a square-packed RUC with the applied boundary conditions.

The process modelling of the square-packed RUC is performed using a series of CUF models with varying levels of refinement within the RUC face, using both 4-node linear (L4) and 9-node quadratic (L9) quad elements. Each CUF model consists of a single linear beam element (B2) along the thickness direction. Two reference 3D-FE models are also developed in Abaqus, where the RUC thickness is represented by a single element. The discretization used in each numerical model is visualized in Fig. 4. The residual stresses in the transverse direction (22-component) that develop within the RUC at the end of the cure cycle, as predicted by the various models, is shown in the form of contour plots in Fig. 5. A summary of all the numerical models, along with the required computational time, is presented in Table 4.
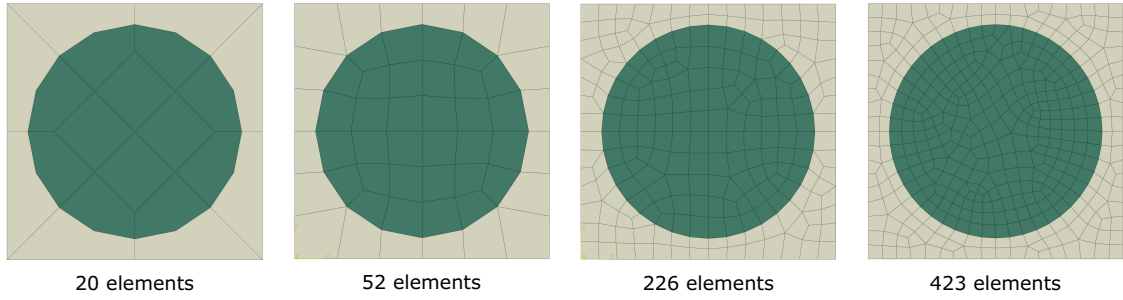
Figure 4: Meshes used in Abaqus and CUF to discretize the square-packed RUC.
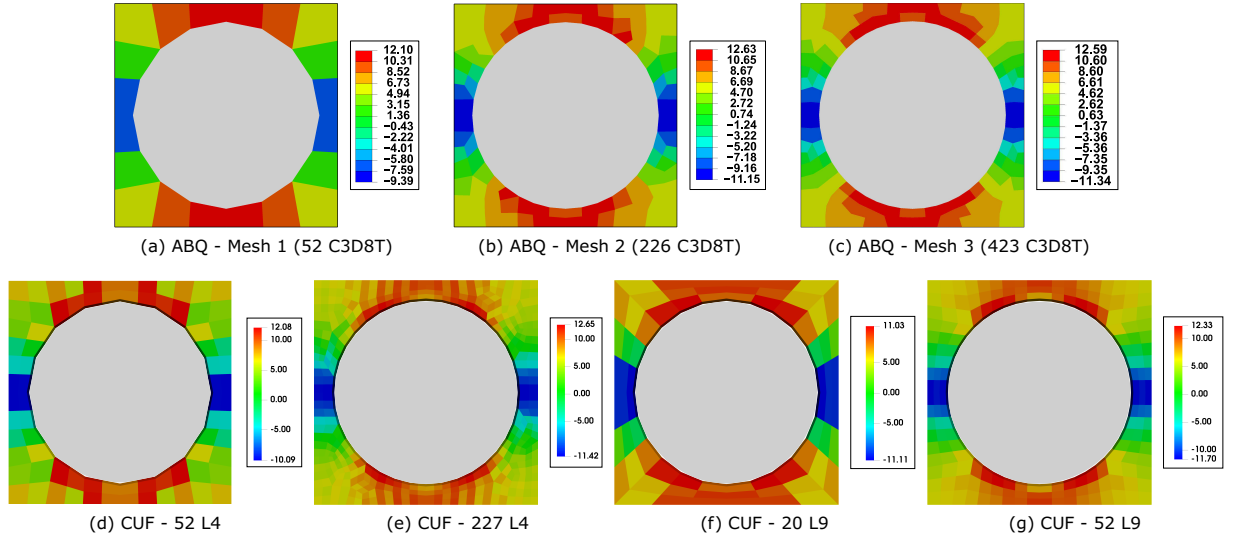
**Figure 5:** Distribution of residual stress (22-component) in the square-packed RUC at the end of cure.

From Fig. 5, it is seen that both the CUF and 3D-FE models are in very good agreement with each other, and provides further verification of the proposed numerical approach. The coarsest models in both cases, i.e. 'ABQ - Mesh 1' and 'CUF - 54 L4', predict very similar stress fields, and are underestimated when compared to the refined models. A similar observation is made for the case of the 'CUF - 20 L9' model, where the predicted stresses are indicative of the intermediate level of refinement within the model. It is also seen that further mesh refinement, in both CUF and 3D-FE, doesn't lead to any significant differences, thereby indicating mesh convergence. Comparing the associated computational time (see Table 4) for the 'ABQ - Mesh 2' analysis with

Table 4: Summary of the numerical models used in the process simulation of the square-packed RUC.

| Model	No. of elements	DOF	Analysis Time [s]
Abaqus - Mesh 1	52 C3D8T	523	40
Abaqus - Mesh 2	226 C3D8T	2,043	52
Abaqus - Mesh 3	423 C3D8T	3,683	68
CUF - Mesh 1	52 L4	520	3.2
CUF - Mesh 2	227 L4	2,048	13.4
CUF - Mesh 3	20 L9	712	4.7
CUF - Mesh 4	52 L9	1,864	14.6

those based on refined CUF (227 L4 and 52 L9), it is seen that the proposed CUF approach is approximately $4x$ as fast as the corresponding 3D-FEA, for similar levels of accuracy.

## 3.2 Curing of RVE with random fiber distribution
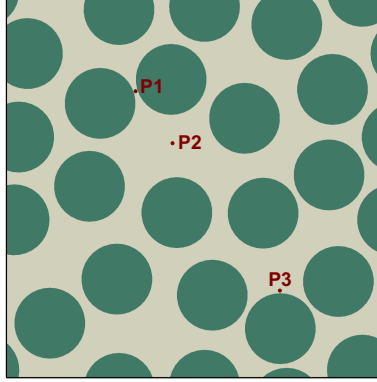
Figure 6: RVE with 20 randomly distributed fibers.

This assessment considers a periodic RVE with 20 randomly distributed fibers, as shown in Fig. 6. The RVE boundary conditions described in Section 3.1 are applied in the current analysis. A series of CUF models is developed with increasing levels of refinement within the RVE face, and a single linear beam element (B2) is used to represent the RVE thickness in each model. Three 3D-FE models are also developed in Abaqus as a numerical reference. The residual stress (22-component) predicted by the models at the end of the cure cycle is presented in Fig. 7. The residual stress evolution at three specific points within the RVE (see Fig. 6), as a function of cure time, is plotted in Fig. 8. A summary of the computational models is presented in Table 5.

From Fig. 7, it is seen that successive refinement of the mesh leads to a converged solution in both the 3D-FE and CUF models. The coarsest models significantly underestimate the compressive stresses that develop at the point P1, which is the matrix region between two neighboring fibers, and thus a zone of considerable stress concentration within the RVE. This can be observed in Fig. 8a, where the 'ABQ - Mesh 1' and 'CUF - 678 L4' models both predict similar magnitudes of the developed residual stress, which is in strong contrast to that predicted by the more refined models. On the other hand, considering the stress evolution at the point P2 (see Fig. 8b), it is seen that all the model predictions are in good general agreement. This is attributed to the
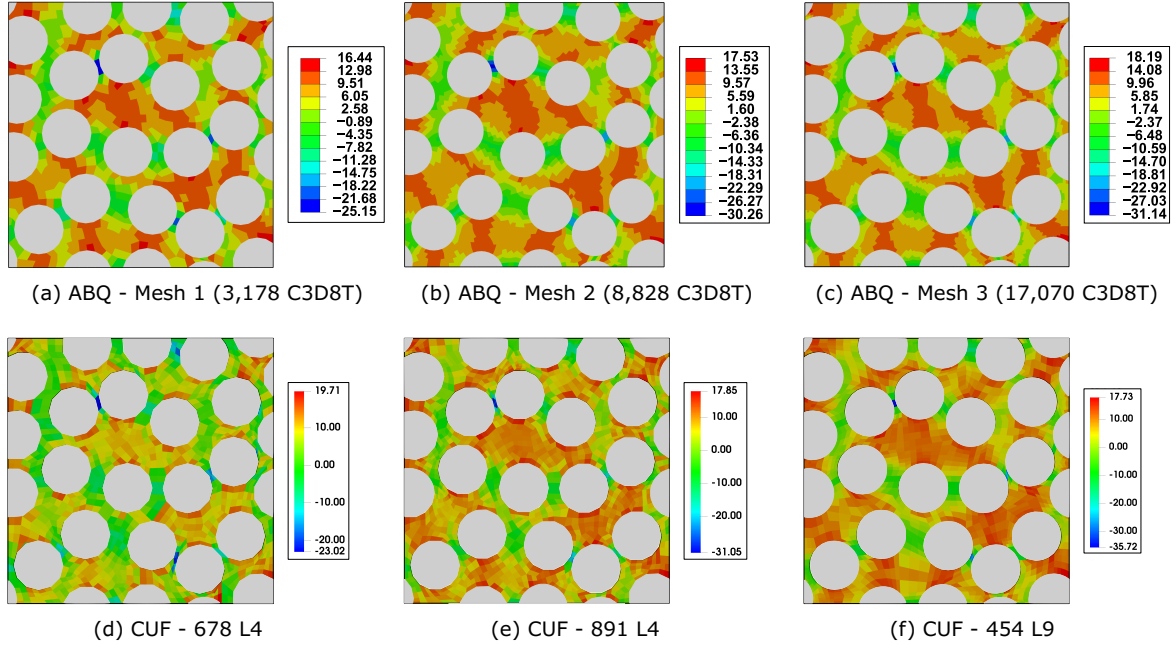
Figure 7: Distribution of residual stress (22-component) in the 20-fiber RVE at the end of cure.
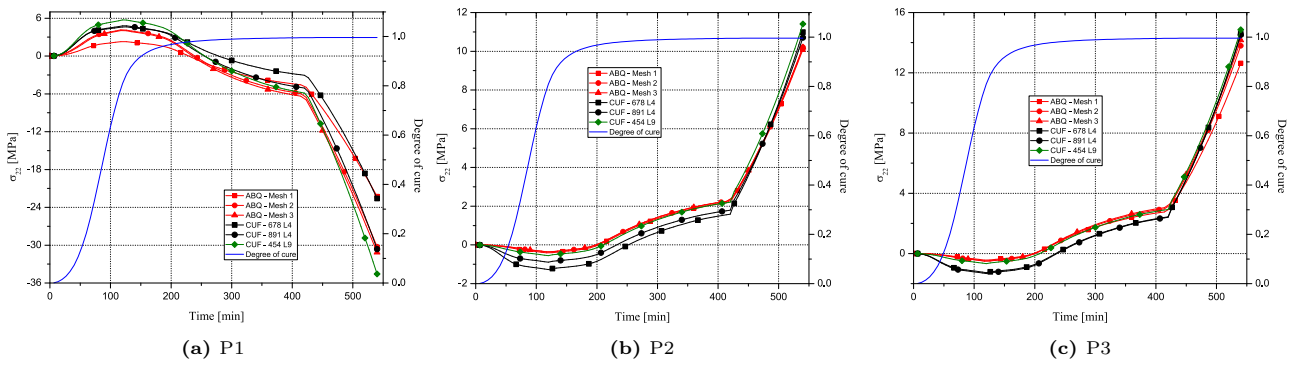
Figure 8: Evolution of residual stress (22-component) as a function of cure time.

fact that the point P2 is situated in a matrix-rich region, and the absence of any stress concentrator implies the sufficiency of a lower mesh density. Finally, examining the residual stress evolution at the point P3 (see Fig. 8c), it is seen that the coarsest 3D-FE model, i.e. 'ABQ - Mesh 1', underestimates the post-cure stress magnitude, and while this is not as inaccurate as in the case of Point P1, still has a considerable error with respect to the refined models. This is explained by the fact that the Point P3 lies in the immediate vicinity of a single fiber which acts as a stress concentrator. The trends observed in the behavior of the 'ABQ - Mesh 1' model at the points P1, P2 and P3 is therefore consistent with the level of stress concentration experienced by the matrix at these points. It is noted that the corresponding coarsest CUF model, i.e. 'CUF - 678 L4', predicts a post-cure residual stress which is in good agreement with that reported by refined models, at the Point P3, inferring that the coarsest CUF model performs better than the corresponding 3D-FE model.

Considering the significant variation in stress concentration at different points within the RVE, which is a consequence of the randomly distributed fibers, any numerical model would require a refined discretization of the matrix component in order to accurately predict the post-cure residual stresses. The 'ABQ - Mesh 2' model is the coarsest 3D-FE model whose results are sufficiently accurate, based on the mesh convergence study. The corresponding CUF model, with an equivalent quality of predicted results, is the 'CUF - 891 L4' model. Comparing the computational costs associated with these two models, see Table 5, it is seen that the CUF approach is approximately $10x$ as fast as the 3D-FE case, and is over $7x$ smaller in computational size based on the number of DOF within the models. An important observation is that the computational efficiency of CUF over 3D-FE, when the model domain is increased from a single-fiber RUC to a 20-fiber RVE, correspondingly increases from approximately $4x$ to $10x$, indicating the superior scalability of CUF. Finally, the 'CUF - 454 L9' model, while very accurate, has an unnecessarily excessive level of kinematic refinement, and the corresponding higher computational cost therefore implies that a sufficiently refined L4 model (such as the 'CUF - 891 L4' model) is preferable over those based on L9, for the current class of problem. It is, however, noted that even the 'CUF - 454 L9' model is about $3.5x$ as fast as the most refined 3D-FE model, i.e. 'ABQ - Mesh 3', and is $6.8x$ smaller in size, demonstrating the computational efficiency of the CUF approach over conventional 3D-FEA.

**Table 5:** Summary of the numerical models used in the process simulation of the 20-fiber RVE.

Model	No. of elements	DOF	Analysis Time [s]
Abaqus - Mesh 1	3,178 C3D8T	19,911	352
Abaqus - Mesh 2	8,828 C3D8T	54,447	830
Abaqus - Mesh 3	17,070 C3D8T	104,403	1622
CUF - Mesh 1	678 L4	5,728	55
CUF - Mesh 2	891 L4	7,432	85
CUF - Mesh 3	454 L9	15,400	463

4 Macroscale Experimental Validation

4.1 Process modeling of $[0_2/90_2]$ flat laminate

This analysis considers a $[0_2/90_2]$ flat laminate composed of AS4 carbon fiber and EPON 862/W resin, and is based on the work by Chen and Zhang [57]. The process modeling setup is schematically shown in Fig. 9(a), and consists of a 101.6x101.6 mm^2 laminate placed at the center of a 304.8x304.8 mm^2 aluminum tool. The material properties of AS4 carbon fiber and EPON 862/W resin have been listed in Table 6 and Table 7, respectively, while the cure kinetics parameters for the EPON 862/W is summarized in Table 8.

The CUF model of the test geometry, including both the aluminum tool and the composite laminate, is shown schematically in Fig. 9(b). The tool/part interface is modeled as a shear layer consisting of a single layer of elements. The entire geometry is modeled along the x-axis using 14 linear B2 elements. The tool and shear layer cross-sections (y-z plane) are modelled using 14 linear L4 elements each, while the composite laminate section is discretized with 16 L4 linear elements. Plies with the same orientation have been modeled using a single section element in the thickness direction (z-axis). During the curing process, the bottom surface of the tool is fully constrained, and a temperature boundary condition is prescribed on it according to the cure cycle described in Ref. [57]. Symmetry conditions are applied on the composite part during the tool removal procedure.

(a) Flat laminate schematic　　　　　　　　(b) CUF model
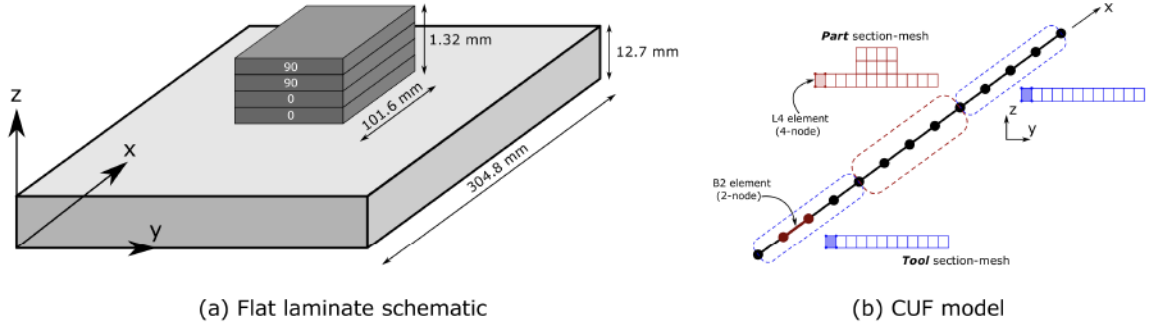
Figure 9: (a) Schematic representation of the $[0_2/90_2]$ flat laminate with tool, (b) CUF model used in the macro-scale process analysis.

The described CUF model is used to perform the curing simulation, and subsequently, the tool removal step to evaluate the final warped profile of the laminate. The vertical deflection (u_z) distribution of the laminate is visualized as a contour plot in Fig. 10a. The predicted CUF solution is compared with reference experimental and numerical data from [57], and is presented in Fig, 10b.

The obtained results show excellent agreement between modeling efforts and experimental results provided by [57], and serves as a validation case for the proposed numerical approach. Numerical predictions suggest that

Table 6: Elastic and thermal material properties of AS4 carbon fiber [57].

Material Property	Value
Density ρ^f	1790.0 $[kg/m^3]$
Axial modulus E_{11}^f	231.0 $[GPa]$
Transverse modulus E_{22}^f, E_{33}^f	15.0 $[GPa]$
In-plane Poisson's ratio ν_{12}^f, ν_{13}^f	0.27 $[-]$
Out-of-plane Poisson's ratio ν_{23}^f	0.25 $[-]$
In-plane shear modulus G_{12}^f, G_{13}^f	24.0 $[GPa]$
Out-of-plane shear modulus G_{23}^f	5.01 $[GPa]$
Axial coefficient of thermal expansion (CTE) α_{11}^f	-9.0E-7 $[K^{-1}]$
Transverse CTE α_{22}^f, α_{33}^f	7.2E-6 $[K^{-1}]$
Axial thermal conductivity κ_{11}^f	6.83 $[W/mK]$
Transverse thermal conductivity κ_{22}^f, κ_{33}^f	2.18 $[K^{-1}]$
Specific heat c_p^f	1134.0 $[J/kgK]$

**Table 7:** Elastic and thermal material properties of EPON 862/W epoxy resin [57].

Material Property	Value
Density ρ^m	1300.0 $[kg/m^3]$
Elastic modulus E^m	2230.0 $[MPa]$
Poisson's ratio ν^m	0.36 $[MPa]$
Coefficient of thermal expansion α^m	1.85E-4 $[K^{-1}]$ (above T_g)
	7.78E-5 $[K^{-1}]$ (below T_g)
Coefficient of chemical shrinkage β^m	0.111 $[-]$
Thermal conductivity κ^m	0.148 $[W/mK]$
Specific heat c_p^m	1219.0 $[J/kgK]$

accurate evolution of the thermo-mechanical properties are fundamental to enhance the prediction of residual stress and strain after demolding. The same numerical assessment has been repeated, considering the RIM R135/H1366 epoxy system (see Section 2.1). Figure 11 shows results of the process modeling simulations for the RIM R135/H1366 flat laminate virtually manufactured using the proposed approach.
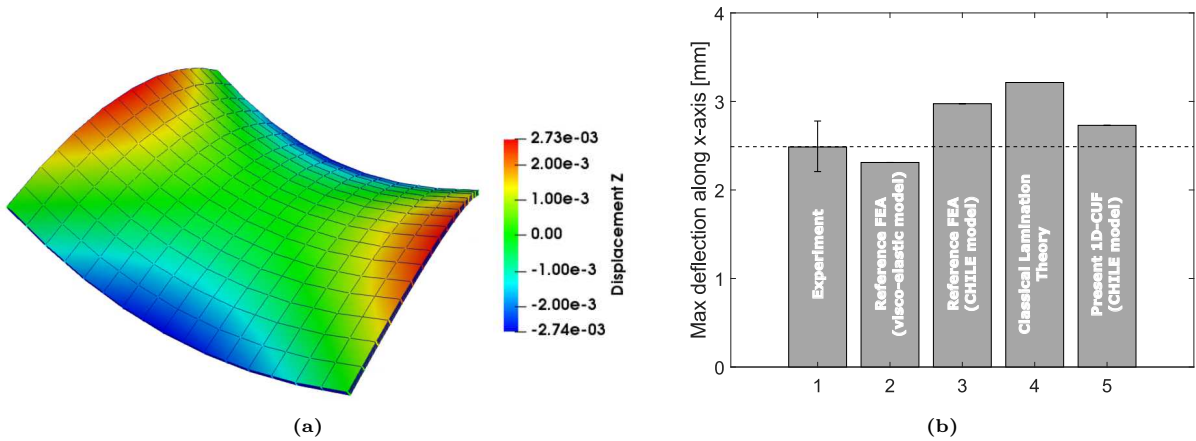
Figure 10: (a) CUF prediction of the vertical deflection of the EPON 862/W flat laminate after the curing and tool-removal process (5x scale-factor), and (b) Comparison of CUF predictions of the maximum deflection with reference experimental and numerical data [57].

Table 8: Cure kinetics parameters for EPON 862/W epoxy resin [57].

Cure kinetic parameter	Value
Exponent m	0.4 $[-]$
Exponent n	1.65 $[-]$
Rate constant A_1	$-$
Rate constant A_2	7098 $[s^{-1}]$
Activation energy ΔE_1	-
Activation energy ΔE_2	5.5E4 $[J]$
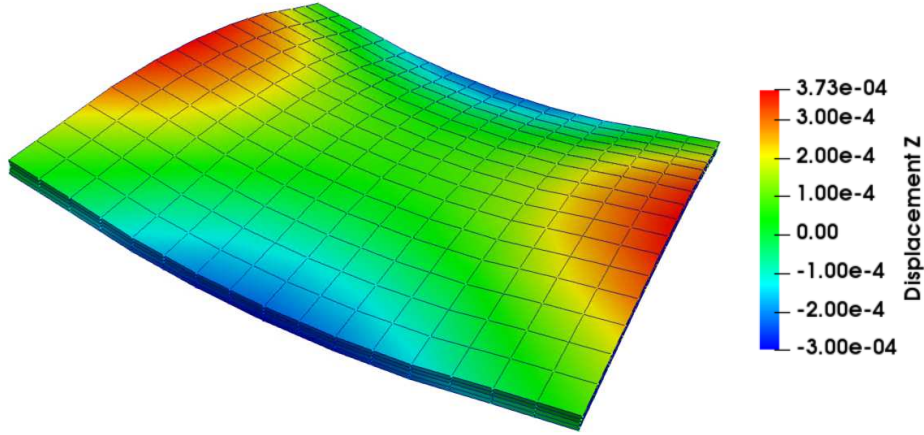
Figure 11: CUF prediction of the vertical deflection of the RIM R135/H1366 flat laminate after the curing and tool-removal process ($5x$ scale-factor).

5   Conclusion

A numerical approach based on the Carrera Unified Formulation (CUF) has been proposed for the curing analysis of thermoset fiber-reinforced composites at the micro-scale, and the prediction of residual stresses that develop during the cure cycle. A description of the thermoset process model and CUF structural modeling is presented, along with an overview of their combination which is used to simulate the curing process for a prescribed cure cycle. A set of numerical assessments has been considered as verification cases, where the CUF approach is compared with reference 3D finite element models developed in Abaqus. The assessed cases include a single-fiber repeating unit cell and a 20-fiber representative volume element, and demonstrate the accuracy of the CUF models. It is also shown that CUF models exhibit an order-of-magnitude higher computational efficiency – in terms of analysis time – than 3D-FE models, for comparable levels of accuracy. By comparing the computational costs of the two numerical methods for the single-fiber RUC and 20-fiber RVE cases, it is seen that CUF scales better than 3D-FEA as the structural size is increased. Such advantages, inherent to CUF, make it a strong candidate in applications such as virtual manufacturing and testing with a multiscale resolution, which fall under the scope of Integrated Computational Materials Engineering (ICME). The experimental validation of the 0/90 laminate at the macroscale shows that accurate material characterization as function of time is needed to predict residual stress in a computational efficient way within 9% accuracy.

6   Acknowledgments

References

[1] Miroslav Stojkovic and Javaid Butt. Industry 4.0 implementation framework for the composite manufacturing industry. *Journal of Composites Science*, 6(9), 2022.

[2] Olivia J. Pinon Fischer, John F. Matlik, William D. Schindel, Mathew O. French, Mohammed H. Kabir, Jayendra S. Ganguli, Martin Hardwick, Steven M. Arnold, Alan D. Byar, Jung-Ho Lewe, Sankara Mahadevan, Scott Duncan, John J. Dong, Don A. Kinard, and Marianna Maiaru. Digital twin: Reference model, realizations, and recommendations. *INSIGHT*, 25(1):50–55, 2022.

[3] I. Baran, K. Cinar, N. Ersoy, R. Akkerman, and J. H. Hattel. A review on the mechanical modeling of composite manufacturing processes. *Archives of computational methods in engineering*, 24(2):365–395, 2017.

[4] K. S. Kim and H. T. Hahn. Residual stress development during processing of graphite/epoxy composites. *Composites Science and Technology*, 36(2):121–132, 1989.

[5] Y. A. Chekanov, V. N. Korotkov, B. A. Rozenberg, E. A. Dhzavadyan, and L. M. Bogdanova. Cure shrinkage defects in epoxy resins. *Polymer*, 36(10):2013–2017, 1995.

[6] H. Hu, D. Cao, M. Pavier, Y. Zhong, L. Zu, L. Liu, and S. Li. Investigation of non-uniform gelation effects on residual stresses of thick laminates based on tailed fbg sensor. *Composite Structures*, 202:1361–1372, 2018.

[7] J. Fish, G. J. Wagner, and S. Keten. Mesoscopic and multiscale modelling in materials. *Nature materials*, 20(6):774–786, 2021.

[8] Z. Yuan, V. Aitharaju, and J. Fish. A coupled thermo-chemo-mechanical reduced-order multiscale model for predicting process-induced distortions, residual stresses, and strength. *International Journal for Numerical Methods in Engineering*, 121(7):1440–1455, 2020.

[9] Z. Yuan, S. Felder, S. Reese, J.-W. Simon, and J. Fish. A coupled thermo-chemo-mechanical reduced-order multiscale model for predicting residual stresses in fibre reinforced semi-crystalline polymer composites. *International Journal for Multiscale Computational Engineering*, 18(5), 2020.

[10] S. Patil, S. Shah, P. Deshpande, K. Kashmari, M. Olaya, G. Odegard, and M. Maiaru. Multi-scale approach to predict cure-induced residual stresses in an epoxy system. In *Proceedings of the American Society for Composites â Thirty-fifth Technical Conference*, 2020.

[11] S. Shah, S. Patil, P. Deshpande, A. Krieg, K. Kashmari, H. Al Mahmud, J. King, G. M. Odegard, and M. Maiaru. Multiscale modeling for virtual manufacturing of thermoset composites. In *AIAA Scitech 2020 Forum*, page 0882, 2020.

[12] P. P. Deshpande, S. Shah, S. Patil, K. Kashmari, M. Olaya, G. M. Odegard, and M. Maiaru. Multiscale modelling of the cure process in thermoset polymers using icme. In *Proceedings of the American Society for Composites â Thirty-fifth Technical Conference*, 2020.

[13] R. J. D'Mello, A. M. Waas, M. Maiaru, and R. Koon. Integrated computational modeling for efficient material and process design for composite aerospace structures. In *AIAA Scitech 2020 Forum*, page 0655, 2020.

[14] P. S. Gaikwad, A. S. Krieg, P. P. Deshpande, S. U. Patil, J. A. King, M. Maiaru, and G. M. Odegard. Understanding the origin of the low cure shrinkage of polybenzoxazine resin by computational simulation. *ACS Applied Polymer Materials*, 3(12):6407–6415, 2021.

[15] G. M. Odegard, S. U. Patil, P. P. Deshpande, K. Kanhaiya, J. J. Winetrout, H. Heinz, S. P. Shah, and M. Maiaru. Molecular dynamics modeling of epoxy resins using the reactive interface force field. *Macromolecules*, 54(21):9815–9824, 2021.

[16] S. U. Patil, S. P. Shah, M. Olaya, P. P. Deshpande, M. Maiaru, and G. M. Odegard. Reactive molecular dynamics simulation of epoxy for the full cross-linking process. *ACS Applied Polymer Materials*, 3(11):5788–5797, 2021.

[17] S. U. Patil, S. P. Shah, M. Olaya, P. P. Deshpande, M. Maiaru, and G. M. Odegard. Molecular dynamics study to predict thermo-mechanical properties of dgebf/detda epoxy as a function of crosslinking density. *arXiv preprint arXiv:2108.00933*, 2021.

[18] M. J. Schey, T. Beke, L. Appel, S. Zabler, S. Shah, J. Hu, F. Liu, M. Maiaru, and S. Stapleton. Identification and quantification of 3d fiber clusters in fiber-reinforced composite materials. *JOM*, 73(7):2129–2142, 2021.

[19] L. Bouaoune, Y. Brunet, A. El Moumen, T. Kanit, and H. Mazouz. Random versus periodic microstructures for elasticity of fibers reinforced composites. *Composites Part B: Engineering*, 103:68–73, 2016.

[20] M. Maiarù, R. J. D'Mello, and A. M. Waas. Characterization of intralaminar strengths of virtually cured polymer matrix composites. *Composites Part B: Engineering*, 149:285–295, 2018.

[21] S. P. Shah, S. U. Patil, C. J. Hansen, G. M. Odegard, and M. Maiaru. Process modeling and characterization of thermoset composites for residual stress prediction. *Mechanics of Advanced Materials and Structures*, pages 1–12, 2021.

[22] S. Shah and M. Maiaru. Microscale analysis of virtually cured polymer matrix composites accounting for uncertainty in matrix properties during manufacturing. In *Proceedings of the American Society for Composites â Thirty-third Technical Conference*, 2018.

[23] M. Maiaru. Effect of uncertainty in matrix fracture properties on the transverse strength of fiber reinforced polymer matrix composites. In *2018 AIAA/ASCE/AHS/ASC Structures, Structural Dynamics, and Materials Conference*, page 1901, 2018.

[24] R. J. DMello and A. M. Waas. Influence of unit cell size and fiber packing on the transverse tensile response of fiber reinforced composites. *Materials*, 12(16):2565, 2019.

[25] E. J. Pineda, B. A. Bednarcyk, A. M. Waas, and S. M. Arnold. Progressive failure of a unidirectional fiber-reinforced composite using the method of cells: Discretization objective computational results. *International Journal of Solids and Structures*, 50(9):1203–1216, 2013.

[26] C. González and J. LLorca. Mechanical behavior of unidirectional fiber-reinforced polymers under transverse compression: Microscopic mechanisms and modeling. *Composites Science and Technology*, 67(13):2795–2806, 2007.

[27] S. Zhang, Y. Xu, and W. Zhang. A novel micromechanical model to study the influence of cure process on the in-plane tensile properties of z-pinned laminates. *Composite Structures*, 300:116156, 2022.

[28] M. Herráez, C. González, C. S. Lopes, R. G. De Villoria, J. LLorca, T. Varela, and J. Sánchez. Computational micromechanics evaluation of the effect of fibre shape on the transverse strength of unidirectional composites: an approach to virtual materials design. *Composites Part A: Applied Science and Manufacturing*, 91:484–492, 2016.

[29] C. J. R. Kosztowny and A. M. Waas. Postbuckling response of unitized stiffened textile composite panels: Experiments. *International Journal of Non-Linear Mechanics*, 137:103814, 2021.

[30] R. J. DMello and A. M. Waas. Virtual curing of textile polymer matrix composites. *Composite Structures*, 178:455–466, 2017.

[31] M. I. Okereke, A. I. Akpoyomare, and M. S. Bingley. Virtual testing of advanced composites, cellular materials and biomaterials: a review. *Composites Part B: Engineering*, 60:637–662, 2014.

[32] D. J. O'Brien, P. T. Mather, and S. R. White. Viscoelastic properties of an epoxy resin during cure. *Journal of composite materials*, 35(10):883–904, 2001.

[33] J. M. Kenny. Determination of autocatalytic kinetic model parameters describing thermoset cure. *Journal of Applied Polymer Science*, 51(4):761–764, 1994.

[34] A. Yousefi, P. G. Lafleur, and R. Gauvin. Kinetic studies of thermoset cure reactions: a review. *Polymer Composites*, 18(2):157–168, 1997.

[35] M. R. Kamal and S. Sourour. Kinetics and thermal characterization of thermoset cure. *Polymer Engineering & Science*, 13(1):59–64, 1973.

[36] A. Ding, S. Li, J. Wang, and L. Zu. A three-dimensional thermo-viscoelastic analysis of process-induced residual stress in composite laminates. *Composite Structures*, 129:60–69, 2015.

[37] X. Hui, Y. Xu, J. Wang, and W. Zhang. Microscale viscoplastic analysis of unidirectional cfrp composites under the influence of curing process. *Composite Structures*, 266:113786, 2021.

[38] E. Carrera, M. Cinefra, M. Petrolo, and E. Zappino. *Finite element analysis of structures through unified formulation*. John Wiley & Sons, 2014.

[39] M. H. Nagaraj, J. Reiner, R. Vaziri, E. Carrera, and M. Petrolo. Progressive damage analysis of composite structures using higher-order layer-wise elements. *Composites Part B: Engineering*, 190:107921, 2020.

[40] M. H. Nagaraj, J. Reiner, R. Vaziri, E. Carrera, and M. Petrolo. Compressive damage modeling of fiber-reinforced composite laminates using 2d higher-order layer-wise models. *Composites Part B: Engineering*, 215:108753, 2021.

[41] M. H. Nagaraj, E. Carrera, and M. Petrolo. Progressive damage analysis of composite laminates subjected to low-velocity impact using 2d layer-wise structural models. *International Journal of Non-Linear Mechanics*, 127:103591, 2020.

[42] I. Kaleel, M. Petrolo, A. M. Waas, and E. Carrera. Computationally efficient, high-fidelity micromechanics framework using refined 1d models. *Composite Structures*, 181:358–367, 2017.

[43] I. Kaleel, M. Petrolo, A. M. Waas, and E. Carrera. Micromechanical progressive failure analysis of fiber-reinforced composite using refined beam models. *Journal of Applied Mechanics*, 85(2), 2018.

[44] M. Maiarú, M. Petrolo, and E. Carrera. Evaluation of energy and failure parameters in composite structures via a component-wise approach. *Composites Part B: Engineering*, 108:53–64, 2017.

[45] E. Carrera, M. Petrolo, M. H. Nagaraj, and M. Delicata. Evaluation of the influence of voids on 3d representative volume elements of fiber-reinforced polymer composites using cuf micromechanics. *Composite Structures*, 254:112833, 2020.

[46] E. Zappino, N. Zobeiry, M. Petrolo, R. Vaziri, E. Carrera, and A. Poursartip. Analysis of process-induced deformations and residual stresses in curved composite parts considering transverse shear stress and thickness stretching. *Composite Structures*, 241:112057, 2020.

[47] S. P. Shah and M. Maiarù. Effect of manufacturing on the transverse response of polymer matrix composites. *Polymers*, 13(15):2491, 2021.

[48] E. Carrera and G. Giunta. Refined beam theories based on a unified formulation. *International Journal of Applied Mechanics*, 2(01):117–143, 2010.

[49] E. Carrera and M. Petrolo. Refined beam elements with only displacement variables and plate/shell capabilities. *Meccanica*, 47(3):537–556, 2012.

[50] E. Zappino, G. Li, A. Pagani, E. Carrera, and A. G. de Miguel. Use of higher-order legendre polynomials for multilayered plate elements with node-dependent kinematics. *Composite Structures*, 202:222–232, 2018.

[51] E. Carrera, M. Filippi, and E. Zappino. Laminated beam analysis by polynomial, trigonometric, exponential and zig-zag theories. *European Journal of Mechanics-A/Solids*, 41:58–69, 2013.

[52] E. Carrera, M. Maiarú, and M. Petrolo. Component-wise analysis of laminated anisotropic composites. *International Journal of Solids and Structures*, 49(13):1839–1851, 2012.

[53] E. Carrera, M. Maiaru, M. Petrolo, and G. Giunta. A refined 1d element for the structural analysis of single and multiple fiber/matrix cells. *Composite Structures*, 96:455–468, 2013.

[54] A. Entezari, M. Filippi, and E. Carrera. Unified finite element approach for generalized coupled thermoelastic analysis of 3d beam-type structures, part 1: Equations and formulation. *Journal of Thermal Stresses*, 40(11):1386–1401, 2017.

[55] T. A. Bogetti and J. W. Gillespie Jr. Process-induced stress and deformation in thick-section thermoset composite laminates. *Journal of composite materials*, 26(5):626–660, 1992.

[56] Andrew Johnston, Reza Vaziri, and Anoush Poursartip. A plane strain model for process-induced deformation of laminated composite structures. *Journal of composite materials*, 35(16):1435–1469, 2001.

[57] W. Chen and D. Zhang. Improved prediction of residual stress induced warpage in thermoset composites using a multiscale thermo-viscoelastic processing model. *Composites Part A: Applied Science and Manufacturing*, 126:105575, 2019.